CHEMISTRY OF MATERIALS

pubs.acs.org/cm Article

Complex Relationship between Side-Chain Polarity, Conductivity, and Thermal Stability in Molecularly Doped Conjugated Polymers

Ban Xuan Dong, Christian Nowak, Jonathan W. Onorato, Tengzhou Ma, Jens Niklas, Oleg G. Poluektov, Garrett Grocke, Mark F. DiTusa, Fernando A. Escobedo, Christine K. Luscombe, Paul F. Nealey, and Shrayesh N. Patel*

Cite This: Chem. Mater. 2021, 33, 741−753 Read Online

ACCESS | Metrics & More | Article Recommendations | Supporting Information

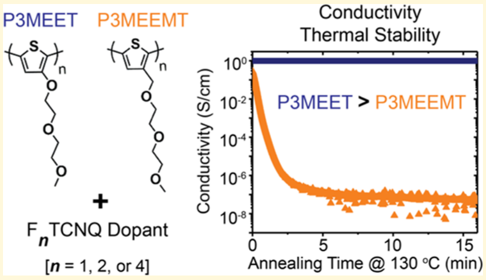

ABSTRACT: Molecularly doped conjugated polymers with polar side chains are an emerging class of conducting materials exhibiting enhanced and thermally stable conductivity. Here, we study the electronic conductivity (σ) and the corresponding thermal stability of two polythiophene derivatives comprising oligoethylene glycol side chains: one having oxygen attached to the thiophene ring (poly(3-(methoxyethoxyethoxy)thiophene) (P3MEET)) and the other having a methylene spacer between the oxygen and the thiophene ring (poly(3-(methoxyethoxyethoxymethyl)thiophene) (P3MEEMT)). Thin films were vapor-doped with fluorinated derivatives of tetracyanoquinodimethane (F_nTCNQ, n = 4, 2, 1) to determine the role of dopant strength (electron affinity) in maximum achievable σ. Specifically, when vapor doping with F_4TCNQ, P3MEET achieved a substantially higher σ of 37.1 ± 10.1 S/cm compared to a σ of 0.82 ± 0.06 S/cm for P3MEEMT. Structural characterization using a combination of X-ray and optical spectroscopy reveals that the higher degree of conformational order of polymer chains in the amorphous domain upon doping with F_4TCNQ in P3MEET is a major contributing factor for the higher σ of P3MEET. Additionally, vapor-doped P3MEET exhibited superior thermal stability compared to P3MEEMT, highlighting that the presence of polar side chains alone does not ensure higher thermal stability. Molecular dynamics simulations indicate that the dopant−side-chain nonbond energy is lower in the P3MEET:F_4TCNQ mixture, suggesting more favorable dopant−side-chain interaction, which is a factor in improving the thermal stability of a polymer/dopant pair. Our results reveal that additional factors such as polymer ionization energy and side-chain−dopant interaction should be taken into account for the design of thermally stable, highly conductive polymers.

1. INTRODUCTION

Conjugated polymers (CPs) have long played a vital role in advancing the organic electronics field owing to their solution processability, mechanical flexibility, and the tunability of their optical and electrical properties via facile molecular design/synthesis strategies.[1−6] In many applications such as organic field-effect transistors (OFETs) or organic photovoltaics (OPVs), doping CPs with molecular dopants has been increasingly explored to fill traps, improve charge injection, and improve carrier mobility, which in total improves device performance.[7−11] For organic thermoelectrics, doping is of particular importance since the physical properties of a thermoelectric material such as electronic conductivity, Seebeck coefficient, and thermal conductivity strongly depend on carrier concentration.[12−14] As such, it is critical to explore strategies that can improve both the doping efficiency and electrical performance for the long-term viability of organic electronic and organic thermoelectric applications.

Doping CPs is usually performed via the addition of molecular dopants to either oxidize (p-type doping) or reduce (n-type doping) the conjugated backbone. One of the most common strategies to improve electronic conductivity (σ) is through the doping method. Sequential doping methods in which prefabricated polymer thin films are exposed to the dopant in the vapor or solution phase[15−21] have been shown to give superior σ compared to the solution coprocessing method[22,23] in which the samples are cast from mixed polymer/dopant solutions. The enhanced performance in samples doped by sequential methods is largely due to the preservation of the underlying structure of the CPs, whereas in the solution coprocessing method, the aggregation of the doped polymers in solution before casting generally results in films with poor quality and low σ. For example, sequential doping of CPs such as poly(3-hexylthiophene) (P3HT)[17,19] or poly[2,5-bis(3-tetradecylthiophen-2-yl)thieno[3,2-*b*]-thiophene] (PBTTT)[24,25] with a small molecule acceptor 2,3,5,6-tetrafluoro-7,7,8,8-tetracyanoquinodimethane

Received: October 27, 2020
Revised: December 16, 2020
Published: January 6, 2021

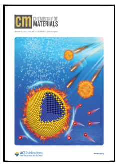

(F_4TCNQ) can result in values of σ several orders of magnitude higher than the solution coprocessing method. In addition to changing the doping method, σ can be enhanced by processing films with a high degree of crystallinity,[20,26] controlling crystallite orientation,[27] or using polymers with intrinsically higher carrier mobility.[24,28,29] Recently, using a combination of the sequential doping method and crystallite orientation control, Brinkmann and co-workers achieved a σ of 2×10^5 S/cm in aligned PBTTT, a record conductivity for modern solution-processable semiconducting polymers.[30]

While considerable efforts have been made to significantly improve the σ of molecularly doped CPs, a certain drawback is their thermally unstable conductivity. It has been reported that F_4TCNQ-doped organic semiconductors are thermally unstable, and σ significantly decreases when the samples are heated above 90 °C through the sublimation-mediated loss of F_4TCNQ either in an inert or ambient air environment.[31,32] Therefore, to enable the use of molecularly doped CPs in applications operating at elevated temperatures, as is the case for thermoelectrics, efforts must also be devoted to circumventing the thermal stability issue of the polymer and dopant pair. To date, a handful of reports directly addressing the thermal stability issues of doped CPs have been published. Li et al. showed that by encapsulating doped samples, the sublimation of F_4TCNQ can be significantly suppressed even upon heating to 100 °C.[33] Yamashita et al. exchanged the F_4TCNQ^- anion in F_4TCNQ-doped PBTTT with anions provided by an ionic liquid solvent and observed a significant enhancement in σ and thermal stability in the case of exchange with hydrophobic closed-shell anions.[34] One potentially important approach that is being increasingly used is polar side-chain engineering. Several reports[31,35,36] demonstrated the use of polythiophene derivatives bearing oligoethylene glycol polar side chains to achieving high conductivity up to 100 S/cm upon doping with F_4TCNQ and high thermal stability up to 150 °C, even in air. While these studies have shown the role of polar side chains in improving the thermal stability of electronic conductivity for molecularly doped polymers, a fundamental question on the nature of the enhancement remains: is it simply the presence of side chains with a polar character that enhances stability or whether other additional factors are in play?

To explore this question, we synthesize two polythiophene derivatives, poly(3-(methoxyethoxyethoxy)thiophene) (P3MEET) and poly(3-(methoxyethoxyethoxymethyl)-thiophene) (P3MEEMT) (Figure 1a), and measure σ and their thermal stability after vapor doping with fluorinated derivatives of tetracyanoquinodimethane (F_nTCNQ, $n = 4, 2, 1$). While both polymers have polar oligoethylene glycol polar side chains, the key difference between them is that the oxygen is directly attached to the thiophene rings in P3MEET, while its analogue P3MEEMT has a methylene spacer between the oxygen and the thiophene ring. In the first part of the paper, we report on the measured σ of both polymers after vapor doping F_nTCNQ and the connection between the ionization energy (IE) of the polymer and the varying electron affinity (EA) of the dopants. Despite possessing almost identical side-chain chemistry, P3MEET exhibits room-temperature σ as high as 37 S/cm upon doping with F_4TCNQ vapor, which is ca. 50 times higher than those of F_4TCNQ-doped P3MEEMT samples. In the second part of the paper, we investigate the origin of the observed higher electronic conductivity of P3MEET:F_4TCNQ through a combination of X-ray scattering and molecular spectroscopy techniques (UV−vis−near-infrared (NIR), electron paramagnetic resonance (EPR), and Raman) complemented with molecular dynamics (MD) simulations. The analysis reveals the role of charge carrier concentration and conformational order of the polymers as factors in enhancing σ. In the third and final part of the paper, we report on the thermal stability of σ of vapor-doped thin films. P3MEET exhibits superior thermal stability with all three dopants compared to P3MEEMT despite both containing oligoethylene glycol polar side chains. This difference in thermal stability highlights that the presence of polar side chains alone does not impart stability in electronic conductivity at elevated temperatures and thus other factors may be in play.

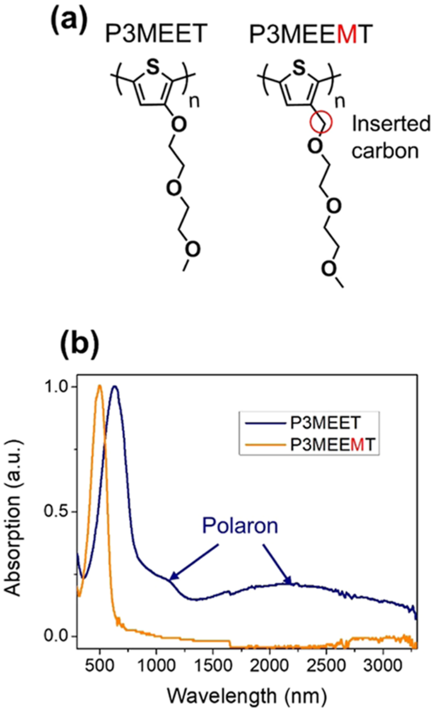

Figure 1. (a) Chemical structures of P3MEET and P3MEEMT. (b) Normalized UV−vis absorption spectra of undoped/neat P3MEET and P3MEEMT thin films fabricated by the spin-casting method.

2. RESULTS AND DISCUSSION

2.1. Chemistry and Optical Spectra of P3MEET and P3MEEMT.

Both P3MEET and P3MEEMT are synthesized using Kumada catalyst transfer polymerization (KCTP), as shown in the Supporting Information (SI) and detailed in our previous publication.[37] The molecular weights (M_n) are 9.2 and 11.2 kg/mol, the dispersity ($Đ$) values are 1.4 and 1.5, and the regioregularity (RR) values are 95 and 94% for P3MEET and P3MEEMT, respectively. The similarities between M_n, $Đ$, and RR of both polymers imply that any differences arising from the two polymers will most likely originate from the difference in side-chain chemistry. Thin films of ca. 50 nm of P3MEET and P3MEEMT were fabricated by spin-casting polymer solutions in chloroform and acetonitrile, respectively. The absorption spectra of P3MEET and P3MEEMT thin films are shown in Figure 1b. In the case of P3MEET, having the oxygen atom right next to the polythiophene backbone results in a marked red shift of the main absorption feature compared to P3MEEMT. This shift is due to the electron-donating ability of the oxygen atom to the thiophene core, which reduces the ionization energy (IE) and lowers the band gap of P3MEET, similar to previous observations in the literature.[35,38] Notably, we observe the signature of polaron absorption peaks in neat P3MEET across several batches that we synthesized, as indicated by the red arrows in Figure 1b. The same feature is absent in P3MEEMT, even though both polymers were synthesized and handled in almost identical ways. The appearance of the polaron peak in the neat P3MEET thin film indicates that P3MEET is "intrinsically" charged. This observation most likely originates from the low ionization energy of P3MEET, which makes this polymer prone to oxidation from ambient air during the synthesis and handling processes. This leads to higher "intrinsic" carrier concentration and conductivity, as will be discussed in the next section.

2.2. Electronic Conductivity of Films Vapor Doped with Fluorinated Derivatives of TCNQ.

Cyclic voltammetry (CV) was used to quantify the approximate ionization energies (IEs) of both P3MEEMT and P3MEET thin films (Figure S2a). The IE of P3MEET is 4.92 eV and the IE of P3MEEMT is 5.45 eV. The electronic conductivity (σ) of P3MEET and P3MEEMT thin films were controlled through the addition of fluorinated derivatives of tetracyanoquinodimethane molecular dopant molecules. These include 2,3,5,6-tetrafluoro-7,7,8,8-tetracyanoquinodimethane (F_4TCNQ), 2,5-difluoro-7,7,8,8-tetracyanoquinodimethane (F_2TCNQ), and 2-fluoro-7,7,8,8-tetracyanoquinodimethane (F_1TCNQ), where the fluorination level controls the electron affinity (EA). Solution CV measurements quantified approximate EA values for F_4TCNQ, F_2TCNQ, and F_1TCNQ to be 5.25 eV, 5.1 eV, and 5.01 eV, respectively (Figure S2b). Expectedly, the EA decreases with decreasing fluorination level.[39] The IEs of P3MEET and P3MEEMT, together with the chemical structures and EAs of the three dopants, are shown in Figure 2a.

To introduce molecular dopants into the host polymer, the vapor doping method was employed where one first casts a thin film and then infiltrates the dopant from the vapor phase, as illustrated in Figure 2b. After 20 min of doping, the dopant is found to fully penetrate through the film thickness for both polymers, as demonstrated by the grazing-incidence wide-angle X-ray scattering (GIWAXS) depth profile experiments (Figure S6). The details of the vapor doping process are provided in Section 4. The lateral, in-plane σ of both polymers as a function of F_nTCNQ (n = 4, 2, and 1) vapor doping time is shown in Figure 2c. Upon vapor doping with F_nTCNQ, the σ of P3MEET and P3MEEMT significantly increases and levels out at ca. 10 min. The plateau σ of P3MEET is 37.1 ± 10.1, 24.9 ± 0.8, and 20.1 ± 0.2 S/cm for F_4TCNQ, F_2TCNQ, and F_1TCNQ vapor-doped films, respectively. While the σ of P3MEET slightly increases with the fluorination level of the dopant, it is notable that σ is within the same order of magnitude. For reference, the σ of P3MEET:F_4TCNQ is comparable to the σ of F_4TCNQ-doped p(g42T-T), a polythiophene derivative bearing polar tetraethylene glycol side chains as reported by Kroon et al.[35] For P3MEEMT, the plateau σ is 0.82 ± 0.06 and 1.6×10^{-3} S/cm for F_4TCNQ and F_2TCNQ vapor-doped films, respectively, while the σ of F_1TCNQ vapor-doped was too low to be measured (within experimental limitations). Overall, P3MEEMT exhibits substantially lower σ compared to P3MEET. Moreover, the σ of P3MEEMT increases significantly with the fluorination level of the dopant, which is in stark contrast to P3MEET.

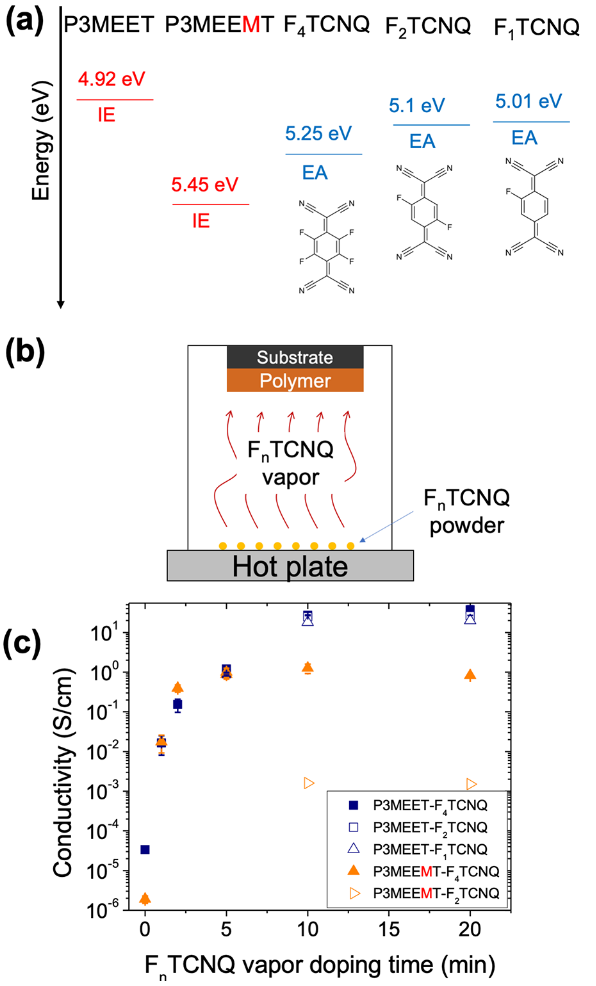

Figure 2. (a) Ionization energies (IEs) of P3MEET and P3MEEMT together with the electron affinities (EAs) of the three dopants F_1TCNQ, F_2TCNQ, and F_4TCNQ used in this work. (b) Schematic representation of the vapor doping process. (c) Electronic conductivity of both polymers as a function of vapor doping time.

The trends in σ for vapor-doped polymers can be further explained through the comparison between the IE of the polymer and the EA of the dopant. As a first approximation, one can take the difference IE − EA to determine the propensity of charge transfer between the polymer and the dopant. IE − EA < 0 indicates that electron transfer is energetically favorable, while IE − EA > 0 indicates that electron transfer is energetically prohibitive. This comparison suggests that all three dopants are energetically favorable for charge transfer with P3MEET, which is consistent with σ being within the same order of magnitude with all three dopants. On the other hand, the greater than 0 difference between IE and EA suggests that all three dopants are energetically prohibitive for charge transfer with P3MEEMT. Despite this, measurable electronic conduction was observed with F_4TCNQ and F_2TCNQ vapor-doped films of P3MEEMT. These results highlight that considering the difference between IE and EA as the charge-transfer driving force is only an approximation and that other factors must also be considered. For instance, recent evidence suggests that the EA of a p-type molecular dopant strongly depends on the molecular host due to intermolecular electrostatic interactions.[40] Moreover, it is important to note that the values of IE and EA are sensitive to the experimental

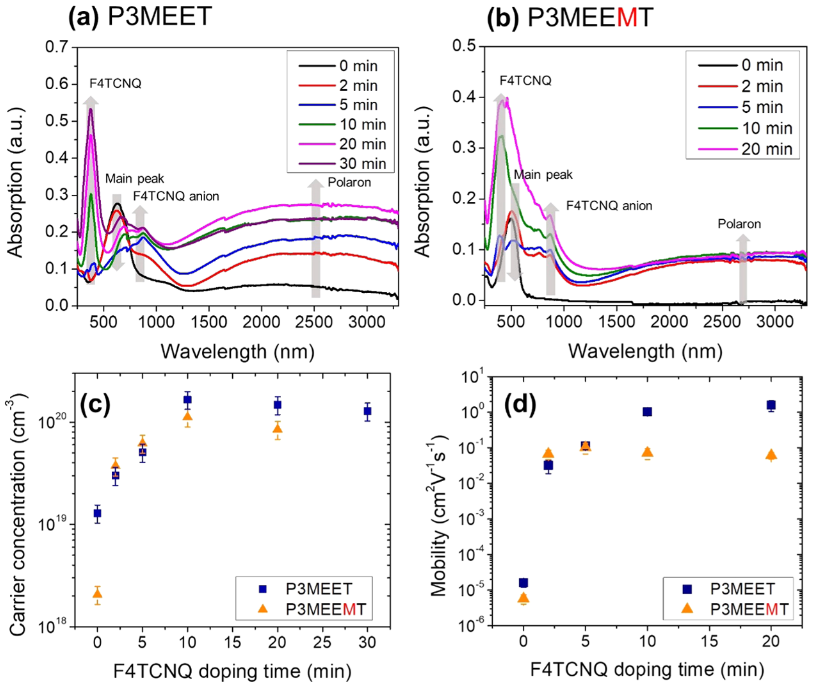

Figure 3. Evolution of UV−vis−NIR absorption spectra as a function of F_4TCNQ doping time for (a) P3MEET and (b) P3MEEMT. (c) Carrier (spin) concentration calculated from EPR spectra (see the SI) as a function of F_4TCNQ doping time for both polymers. (d) Estimated carrier mobility from carrier (spin) concentration and conductivity as a function of F_4TCNQ doping time.

methods (cyclic voltammetry or photoelectron spectroscopy) or computational methods employed, and thus, the reported values are merely estimations. The results of P3MEEMT:F_nTCNQ presented here reiterates that point. In the next section, we only focused on F_4TCNQ for all subsequent experiments, as it is shown to be the most efficient dopant for both P3MEET and P3MEEMT.

2.3. UV−Vis−NIR and EPR Spectroscopy Reveal the Extent of F_4TCNQ Doping. To study the extent of doping and the charge carrier generation process, UV−vis−NIR absorption spectroscopy was performed as a function of F_4TCNQ doping time for P3MEET and P3MEEMT, as shown in Figure 3a,b, respectively. After vapor doping, we observe changes in the intensity of multiple relevant absorption peaks, as indicated by the arrows in Figure 3a,b. For both polymers, the intensities of the absorption peaks of neutral F_4TCNQ (ca. 390 nm), F_4TCNQ anions (ca. 700 nm), and polaron (ca. 2500 nm) increase, whereas the primary polymer absorption peak decreases (ca. 490 nm for P3MEEMT and ca. 640 nm for P3MEET). The appearance of the F_4TCNQ anion absorption peak is indicative of the integer charge transfer (ICT) doping mechanism.[41−43] As discussed earlier, polaron peaks were observed in neat P3MEET thin films. The absorption feature of neat F_4TCNQ most likely originates from the excess amount of vapor dopant either within the polymer film or accumulated on top of the film after extended doping.

Although the general trend is similar for both polymers, we observe some differences between P3MEET and P3MEEMT. The intensity of the polaron absorption peak in P3MEET gradually increases up until 20 min and slightly decreases at 30 min of doping. The polaron peak of P3MEEMT, on the other hand, is found to saturate faster after several minutes of doping. Since the intensity of the polaron peak indicates the degree of ionization of the polymer backbone, this observation indicates a higher degree of doping in P3MEET compared to that in P3MEEMT, which is in good agreement with higher σ in P3MEET. We attempted to deconvolute the absorption spectra to individual absorption peaks for a more rigorous assessment of doping level absorption peaks.[35,42] Peak deconvolution proved to be difficult since strong peak overlapping in our F_4TCNQ-doped P3MEET and P3MEEMT systems prevented us from finding an accurate solution for the fit. However, since the polaron peak near 2500 nm is sufficiently far away from other absorption peaks, we qualitatively conclude that the doping efficiency is slightly higher in P3MEET.

The spin concentration was measured using electron paramagnetic resonance (EPR) spectroscopy to approximate the charge carrier concentration F_4TCNQ-doped P3MEET and P3MEEMT. The continuous-wave (CW) X-band EPR spectra for P3MEET and P3MEEMT thin films vapor doped with F_4TCNQ are shown in Figure S7. The spin concentration of each sample was calculated through double integration of the EPR spectrum, and the volume of the measured film (Figure 3c). The spin concentration of neat P3MEET is $(2.1 \pm 0.4) \times 10^{18}$ cm^{-3}, which is about an order of magnitude higher than the spin concentration $(1.3 \pm 0.3) \times 10^{17}$ cm^{-3} of P3MEEMT. The higher initial spin concentration for neat P3MEET is consistent with the observation of polaron formation through UV−vis−NIR. After vapor doping with F_4TCNQ, the spin concentration increases for both polymers. At 10 min, the maximum spin concentration of P3MEET is $(1.6 \pm 0.3) \times 10^{20}$ cm^{-3}, which is 45% higher than the maximum spin concentration $(1.1 \pm 0.2) \times 10^{20}$ cm^{-3} of P3MEEMT. This difference suggests better F_4TCNQ doping efficiency in P3MEET.

The electronic conductivity σ is a function of charge carrier concentration n and carrier mobility μ according to $\sigma = qn\mu$, where $q = 1.6 \times 10^{-19}$ C is the elementary charge. Therefore, the difference in conductivity between the two polymers may originate from the differences in n and μ. As shown in Figure 3d, the estimation of apparent charge mobility (μ) was calculated as a function of F_4TCNQ doping time using the measured value of σ (Figure 2c) and spin concentration (Figure 3c) as the value for n. For the neat films, μ for P3MEET is $(1.63 \pm 0.42) \times 10^{-5}$ $cm^2/(V\ s)$, which is higher than $\mu = (5.73 \pm 1.65) \times 10^{-6}$ $cm^2/(V\ s)$ for P3MEEMT, whereas in the saturation regime, the carrier mobility is significantly higher in P3MEET (1.57 ± 0.53 $cm^2/(V\ s)$ in P3MEET vs $(6.07 \pm 1.30) \times 10^{-2}$ $cm^2/(V\ s)$ in P3MEEMT in fully doped samples).

Note that the carrier concentration does not strictly scale linearly with electronic conductivity probably due to the presence of density of states in disordered polymeric semiconductors, which gives rise to mobile and immobile carriers.[44,45] The total amount of carriers measured by EPR thus does not necessarily reflect the amount of mobile carriers that contribute to conductivity. Moreover, in addition to the carriers generated from polarons on the polymers, there are also other types of paramagnetic species that could be detected by EPR such as "intrinsic" carrier concentration or F_4TCNQ radical anion.[36] It is possible that these types of carriers do not contribute equally to charge transport. Distinguishing the different transport mechanisms for these types of carriers is out of scope for this study.

2.4. GIWAXS and MD Simulations Show Changes in Local Ordering upon Vapor Doping. To characterize the influence of vapor doping on the local order, grazing-incidence wide-angle X-ray scattering (GIWAXS) was performed on P3MEET:F_4TCNQ and P3MEEMT:F_4TCNQ thin films. Shown in Figure 4a−d are two-dimensional (2D) GIWAXS images of P3MEET and P3MEEMT before and after doping with F_4TCNQ for 10 min. Two-dimensional GIWAXS images of films doped at different times can be found in the SI (Figure S3). The scattering patterns of neat P3MEET and P3MEEMT appear qualitatively similar and show relevant reflections from side-chain stacking (100) and $\pi-\pi$ stacking (010) scattering planes. These reflections also appear in both the horizontal and vertical directions, indicating a mixed face-on/edge-on orientation of polymer crystallites. Additionally, the weak higher-order scattering reflections and diffuse scattering indicate a microstructure of aggregate and disordered domains. After vapor doping with F_4TCNQ, the 2D GIWAXS images of both polymers appear qualitatively similar to the neat films. One noticeable difference is the appearance of new diffraction spots (indicated by red arrows) for the P3MEEMT sample arising from the accumulation of neutral F_4TCNQ on the surface of the polymer film. Notably, despite the weakly aggregated microstructure, the conductivity of P3MEET:F_4TCNQ is high.

To provide a more quantitative picture of the structural evolution upon vapor doping with F_4TCNQ, the relative degree of crystallinity (rDoC) was estimated using a partial pole figure construction method on the (100) reflection, as shown in Figure S4 and described elsewhere.[37,46,47] For each vapor-doped sample, the rDoC is normalized to the rDoC of the neat thin film. Shown in Figure 4e is the normalized rDoC of P3MEET and P3MEEMT as a function of F_4TCNQ vapor doping time. For both polymers, the infiltration of F_4TCNQ is found to decrease the rDoC of both polymers. After 20 min of doping, the rDoC of P3MEET is ca. 13% compared to that of the neat sample, whereas the rDoC of P3MEEMT is ca. 20%. Here, it is worth noting that for the same vapor doping time, the estimated rDoC of P3MEEMT samples is always higher than P3MEET, indicating that the addition of F_4TCNQ vapor to P3MEET has a stronger impact on the polymer crystallinity as compared to P3MEEMT. The lower rDoC of P3MEET samples indicates that the change in crystallinity upon introducing the vapor dopant is likely not the origin of the higher σ in P3MEET compared to P3MEEMT.[26]

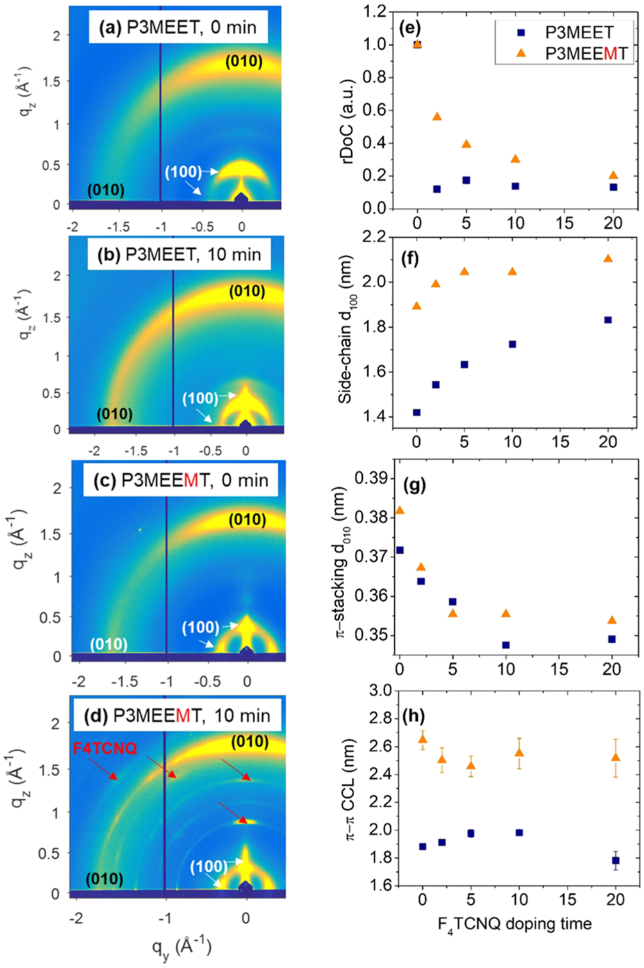

Figure 4. (a−d) Representative GIWAXS patterns of P3MEET and P3MEEMT before and after doping with F_4TCNQ for 10 min. GIWAXS patterns of the polymers at other doping times are shown in the SI. The red arrows indicate diffraction signals of F_4TCNQ crystals. Evolution of (e) relative degree of crystallinity (rDoC), (f) side-chain distance, (g) π-stacking distance, and (h) crystallite coherence length (CCL) along the π-stacking direction upon vapor doping with F_4TCNQ.

To further compare the influence of side-chain chemistry on the polymer−dopant interaction, the side-chain distance $d_{100} = 2\pi/q_{100}$ was calculated as a function of F_4TCNQ doping time (Figure 4f). The value of d_{100} of both polymers increases due to the intercalation of the F_4TCNQ anion into the side-chain region of the aggregate domains, which has been previously observed in other polythiophene-based polymers.[20,26,43] For P3MEEMT, d_{100} increases initially from 1.89 to 2.04 nm but plateaus beyond ca. 10 min of doping. The side-chain distance of neat P3MEET is 1.42 nm, which is smaller than P3MEEMT as expected. Upon introducing F_4TCNQ, the P3MEET side-chain distance continuously increases, with the largest distance of 1.83 nm occurring after 20 min of doping.

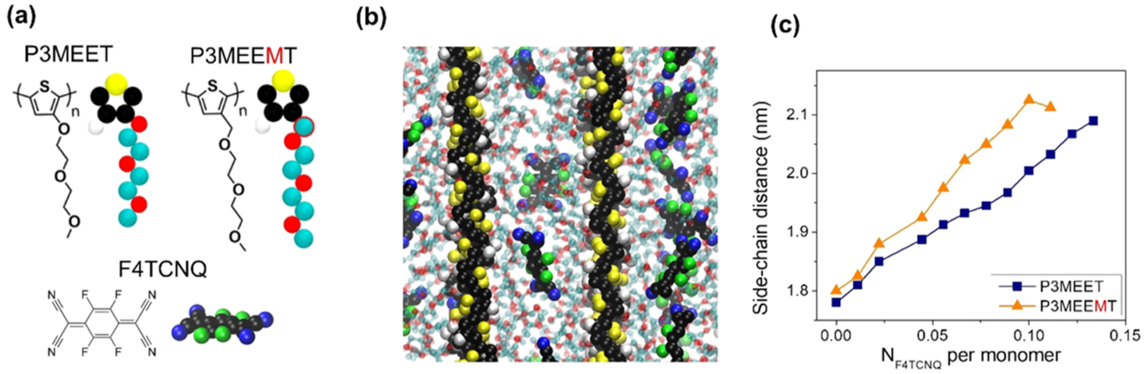

Figure 5. (a) Representation of P3MEET, P3MEEMT, and F_4TCNQ chemical structures used in MD simulations. (b) Exemplary snapshot of F_4TCNQ molecules dispersed within a crystalline domain of P3MEET at a concentration $N_{F_4TCNQ} = 0.0625$. The snapshot of the P3MEEMT−F_4TCNQ structure appears similar and thus is not shown. (c) MD simulation results of crystallite width along the side-chain direction as a function of F_4TCNQ concentration.

Since electronic transport in conjugated polymers strongly depends on $\pi-\pi$ interaction between polymer chains, we investigate the π-stacking distance d_{010} and crystallite coherence length (CCL) along the π-stacking direction of both polymers upon doping. As shown in Figure 4g, for both polymers, d_{010} is found to decrease upon doping. The decrease in the π-stacking distance upon doping is also a widely observed phenomenon for electrochemically and molecularly doped conjugated polymers.[26,43,48−51] While the intercalation of F_4TCNQ into the π-stacks was suggested in early studies,[17,43,52] recent experimental evidence has questioned this hypothesis due to the weak localization of polaron and the lack of X-ray diffraction signals from F4TCNQ-conjugated segment cocrystals.[26] Additionally, the change in $\pi-\pi$ spacing was not observed upon blending conjugated polymers with redox nonactive species such as TCNQ or LiTFSI,[37] implying that reduction of the π-stacking distance is not due to the expansion in the side-chain direction but rather relating to the doping process itself. Therefore, it has been proposed that doping-induced polaron delocalization between adjacent chains leads to attractive forces that reduce $\pi-\pi$ spacing between adjacent chains.[53] It would thus follow that d_{010} decreases upon doping for both P3MEET and P3MEEMT. The final plateau π-stacking distance is lower in P3MEET compared to that in P3MEEMT, which arises from differences in the degree of ionization of the conjugated backbone.

The CCL along the π-stacking direction as calculated from the full width at half-maximum using the Scherrer equation is shown in Figure 4h. While there is no clear trend of CCL as a function of F_4TCNQ doping time, the CCL of P3MEEMT is always higher than that of P3MEET. The CCL of P3MEEMT corresponds to an average of ∼7 π-stacking units, whereas the average π-stacking units in P3MEET is ∼5. This observation suggests that P3MEEMT possesses higher degree of order in the π-stacking direction, consistent with prior observations from differential scanning calorimetry (DSC) measurements that indicate that P3MEEMT is more crystalline than P3MEET.[37,54] The lower $\pi-\pi$ CCL of P3MEET samples also indicates that the difference in CCL of the two polymers is likely not the origin of the higher σ in P3MEET compared to that in P3MEEMT.

To gather additional details of the polymer crystallite−dopant interaction, we employ MD simulations to investigate the neutral dopant distribution within P3MEET and P3MEEMT crystallites. A complete description of our computational methods is given in the SI. Here, we specifically look to see how each P3MEET and P3MEEMT crystalline system responds to the addition of neutral F_4TCNQ. We note that a rigorous investigation of semicrystalline polymer/dopant interactions should involve a study on a system with (i) coexisting crystalline and amorphous domains and (ii) ionized species (polarons and dopant anions) generated by the F_4TCNQ dopant, whose electrostatic interactions will be different from those in neutral polymer/neutral dopant systems. Unfortunately, simulations involving coexisting crystal−amorphous phases and ionized species entail very challenging undertakings, which are beyond the scope of this work. Nevertheless, we expect that the results from this MD investigation of the polymer crystallite/neutral dopant interaction can still provide insight into some of the underlying reasons for the differences in electrical performances of P3MEET and P3MEEMT as discussed below and elsewhere in this work.

To simulate crystalline systems of P3MEET and P3MEEMT, we follow our previously described procedures, which used the initial configuration equivalent to the crystalline structure of poly(3-hexylthiophene) (P3HT) (isomorph I) except that the crystals of both P3MEET and P3MEEMT were expanded to accommodate the longer side chains.[37] We then perform reverse coarse-graining to generate all-atom configurations from equilibrated coarse-graining configurations and subsequently add neutral F_4TCNQ at different concentrations of N_{F_4TCNQ}. Here, N_{F_4TCNQ} is the number of F4TCNQ molecules per repeating monomer unit. Additional details of the simulation can be found in the SI and also in our previous publication.[37] The chemical representations of both polymers and F_4TCNQ are shown in Figure 5a. Figure 5b provides representative snapshots of the P3MEET−F_4TCNQ crystalline system at concentration $N_{F_4TCNQ} = 0.0625$. The corresponding snapshot of the P3MEEMT−F_4TCNQ system appears qualitatively similar and thus is not shown. Importantly, F_4TCNQ is found to be well dispersed within the P3MEET crystalline matrix, residing exclusively within the side-chain region. No F_4TCNQ is found between the π-stacks, consistent with our conclusion from GIWAXS experimental data. We show in Figure 5c the evolution of crystallite width along the side-chain spacing distance as a function of F_4TCNQ concentration. For both P3MEET and

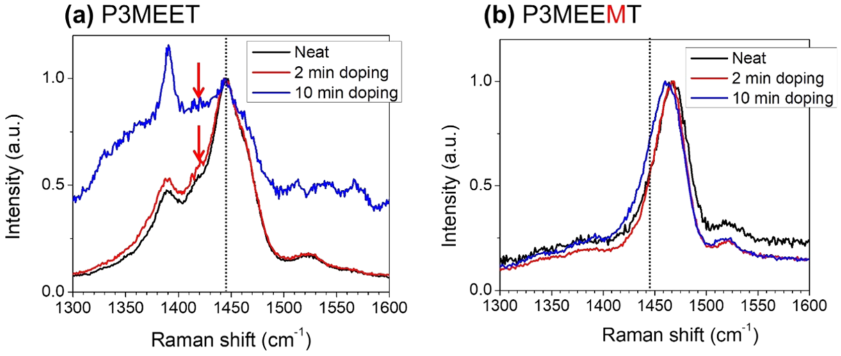

Figure 6. Raman spectra of (a) P3MEET and (b) P3MEEMT at different F_4TCNQ doping times. The arrows in (a) denote the Raman signal from stiffened amorphous chains. The vertical dashed lines in both plots are placed at the same Raman shift for ease of peak position comparison.

P3MEEMT systems, we observe that the side-chain spacing distance calculated from our MD simulations monotonically increases with increasing neutral F_4TCNQ loading, in clear contrast with the experimental data shown in Figure 4f. This behavior is expected as our model only consists of the crystalline phase so that the extra added amount of F_4TCNQ cannot escape into the amorphous phase like the real system and is bound to swell the crystal.

2.5. Raman Spectroscopy Reveals That Extent of Conformational Order Controls the Limits of Electronic Conductivity. Since GIWAXS measurement is only sensitive to ordered domains, information about the amorphous domain before and after doping is not visible by GIWAXS. Considering charge carriers must traverse both aggregate (crystalline) and disordered domains, the amorphous fraction in both P3MEET and P3MEEMT should also play a large role in dictating the limits of macroscopic conductivity. To gain insight into chain conformation in the amorphous domain upon doping, we performed Raman spectroscopy on vapor-doped P3MEET and P3MEEMT thin films. To probe the amorphous part of the samples, the excitation wavelength was selected to be in resonance with the amorphous fraction of the thin film,[55,56] i.e., 532 nm for P3MEET and 473 nm for P3MEEMT. The selection of appropriate wavelength was based on the UV−vis absorption spectra of both the solution and thin film, as depicted and explained in Figure S9.

The normalized Raman spectra of neat and vapor-doped P3MEET and P3MEEMT thin films are shown in Figure 6a,b, respectively. The peak at 1445 cm^{-1} for P3MEET and the peak at 1466 cm^{-1} for P3MEEMT correspond to the intraring symmetric C═C vibrational modes. Here, the Raman spectra were normalized by the intensity of this primary C═C vibrational mode. Additionally, the peak at 1381 cm^{-1} for P3MEET and the weak peak near 1380 cm^{-1} for P3MEEMT correspond to the intraring C−C vibrational mode. Upon closer inspection, besides the main peak near 1445 cm^{-1}, P3MEET's symmetric C═C vibration mode also consists of a small shoulder near 1416 cm^{-1}, as indicated by the red arrows in Figure 6a. As reported for P3HT, a decrease in the wavenumber of the C═C mode arises from neutral polymer chains with increased conformational order (i.e., stiffer and more planar chains).[55,57] In turn, the vibrational mode at 1416 cm^{-1} in P3MEET likely arises from the stiffening of disordered polymer chains in the amorphous regime, whereas the vibrational mode at 1445 cm^{-1} corresponds to polymer chains with a relatively higher degree of conformational order. As a note of reminder, neat P3MEET exhibits polaron formation. Therefore, we attribute the red shift of the main C═C vibration peak in neat P3MEET compared to neat P3MEEMT (note that the dashed lines in Figure 6a,b are placed at the same position for ease of comparison) and together with the appearance of a shoulder near 1416 cm^{-1} to the increased planarity of the polaronic (quinoidal) molecular structure. This is further emphasized by an increase in the relative intensity of the vibrational mode at 1416 cm^{-1} in P3MEET after vapor doping with F_4TCNQ where the concentration of polarons increases.

With respect to P3MEEMT, we observe a red shift of the broad peak at 1466 cm^{-1}, where the shift could stem from the planarization of the polymer backbone upon increasing polaron concentration. However, the final peak position of P3MEEMT at 10 min of doping is 1461 cm^{-1}, which is still higher in wavenumber compared to that of P3MEET, indicating a lower degree of backbone planarization in P3MEEMT. Additionally, a similar shoulder near 1416 cm^{-1} is not observed in P3MEEMT after doping, suggesting the inefficient doping of the amorphous part of P3MEEMT compared to amorphous P3MEET. This difference could be explained by considering the energy mismatch between the polymers and F_4TCNQ. Due to its highly disordered structure, the amorphous part of the semicrystalline conjugated polymers possesses a lower value of IE, rendering it more difficult for p-type charge transfer to occur between the disorded polymer chains and molecular dopants. Therefore, while charge transfer can occur between the polymer crystallite and F_4TCNQ in P3MEEMT, a similar process is not likely to happen in the amorphous regime. In contrast, due to its low IE, charge transfer can still occur between amorphous P3MEET and F_4TCNQ, evident by the stiffening of the polymer chains in the amorphous domain as demonstrated by Raman measurements here. Therefore, stiffer polymer chains in the amorphous domain permitting higher mobility coupled with the higher carrier concentration accounts for the higher conductivity of P3MEET:F_4TCNQ compared to that of P3MEEMT:F_4TCNQ thin films.

2.6. Thermal Stability of Polymer/Dopant Pairs. In addition to high conductivity, the utility of molecularly doped conjugated polymers depends on the polymer's ability to maintain its conductivity at elevated temperatures. Thus, in the final set of experiments, we investigate the thermal stability of vapor-doped polymer thin films in argon and air by measuring the temporal stability of the conductivity at a sufficiently elevated temperature of 130 °C. Shown in Figure 7a is the evolution of conductivity of F_4TCNQ vapor-doped films (10

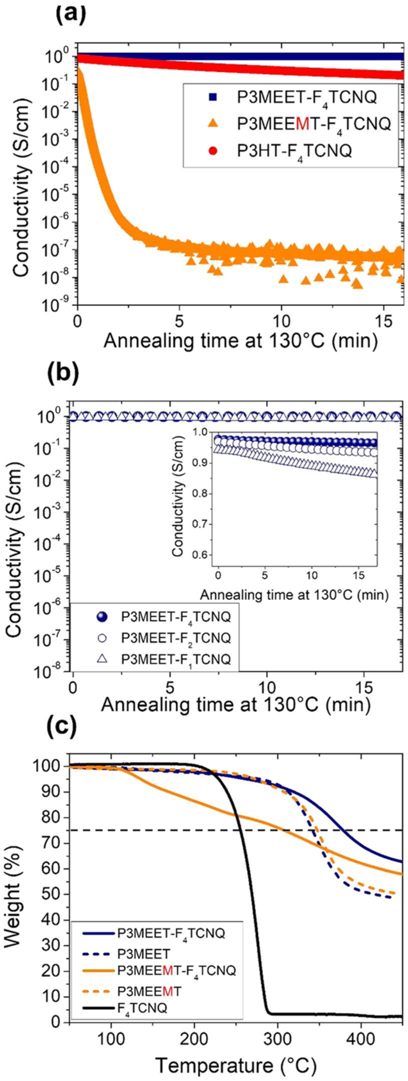

Figure 7. (a) Electronic conductivity of F_4TCNQ-doped P3MEET, P3MEEMT, and P3HT as a function of isothermal annealing time at 130 °C in argon. (b) Electronic conductivity of F_4TCNQ-, F_2TCNQ-, and F_1TCNQ-doped P3MEET as a function of isothermal annealing time at 130 °C in argon. The conductivity was measured on films deposited atop interdigitated electrode (IDE) devices. The inset figure shows the zoom-in plot of the same thermal stability data. (c) Thermogravimetric analysis (TGA) data of P3MEET, P3MEEMT, and F_4TCNQ together with P3MEEMT and P3MEET samples blended with ca. 25 wt % F_4TCNQ. The dashed line represents this 25 wt % from F_4TCNQ.

min) of P3MEET, P3MEEMT, and P3HT as a function of heating time in an argon glovebox. As shown in Figure 7a, after 15 min of heating at 130 °C, the P3MEET:F_4TCNQ sample exhibits only a 1% decrease in conductivity, whereas the P3MEEMT:F_4TCNQ sample exhibits 8 orders of magnitude drop in conductivity. For comparison to a nonpolar side chain, we included an F_4TCNQ-doped P3HT sample, which showed a 75% drop in conductivity after 15 min of annealing and is thus more thermally stable than P3MEEMT:F_4TCNQ. These results emphasize that only adding polar character to the side chain does not impart thermal stability of the conductivity and can in fact reduce the stability. With respect to other molecular dopants, P3MEET vapor doped with F_2TCNQ and F_1TCNQ yielded a similar level of thermal stability to F_4TCNQ-doped films, as demonstrated in Figure 7b. Upon closer examination (see the inset of Figure 7b), we found decreases of 4 and 9% in conductivity for P3MEET:F_2TCNQ and P3MEET:F_1TCNQ, respectively. These numbers are very close to the thermal stability of the P3MEET:F_4TCNQ sample (showed a 1% drop in conductivity under identical conditions) and substantially higher than P3MEEMT:F_4TCNQ and P3HT:F_4TCNQ samples. These results indicate that the thermal stability is insensitive to the magnitude of differences between the IE and EA with F_2TCNQ and F_1TCNQ and consistent with the fact that F_2TCNQ and F_1TCNQ are efficient dopants for P3MEET.

To further demonstrate the superior thermal stability of P3MEET:F_4TCNQ, heating experiments were performed in an ambient air environment. The conductivity of P3MEET:F_4TCNQ exhibited a decrease of ca. 6% at 130 °C after 15 min (Figure S8). Additionally, the conductivity decreased ca. 0.5, 9, and 11% after heating at 100, 150, and 180 °C, respectively (Figure S8). The superior thermal stability of P3MEET:F_4TCNQ in air is similar to the results of Kroon et al., where the same oligoethylene glycol side chains bearing polythiophene, p(g42T-T):F_4TCNQ, was shown to have much better thermal stability compared to P3HT:F_4TCNQ.[31,35] The authors suggested that the thermal stability of p(g42T-T):F_4TCNQ originated from the enhanced "binding" between the oligoethylene glycol side chain and F_4TCNQ. However, despite possessing a nearly identical side chain to P3MEET, the P3MEEMT:F_4TCNQ film shows much inferior thermal stability. Moreover, the P3MEEMT:F_4TCNQ film exhibits less stability to purely aliphatic-side-chain-containing P3HT:F4TCNQ films. In air, the conductivity of P3MEEMT:F_4TCNQ decreases by almost 9 orders of magnitude only after 5 min of annealing. Indeed, there has been a recent report showing that bearing a polar side chain is not necessarily responsible for the enhanced thermal stability of molecularly doped CPs.[58] These results suggest additional factors are responsible for the improved thermal stability in thiophene-based polymers bearing polar sides chains such as our P3MEET and reported p(g42T-T):F_4TCNQ-doped samples.

To determine whether the decrease in conductivity upon heating was from the sublimation of dopant molecules, we performed thermogravimetric analysis (TGA) experiments on neat P3MEET and P3MEEMT, F_4TCNQ powder, and P3MEET and P3MEEMT samples blended with ca. 25 wt % F_4TCNQ. As seen in Figure 7c, neat P3MEET and P3MEEMT show almost identical TGA profiles, with the majority of weight loss occurring at temperatures above 350 °C due to the degradation of the polymers. On the other hand, F_4TCNQ shows an onset of weight loss around 200 °C arising from the sublimation of F_4TCNQ.[20] For the P3MEEMT:F_4TCNQ blend, we observe an early onset of weight loss at 100 °C. The weight loss likely arises from the sublimation of F_4TCNQ molecules after returning to their neutral state due to the instability of the charge state of the P3MEEMT:F_4TCNQ blend. The lower sublimation temperature of F_4TCNQ in the blend arises from differences in the sublimation behavior of a powder and when embedded in a polymer matrix. Overall, the return to the neutral state and sublimation of F_4TCNQ leads to a decrease in the conductivity of P3MEET:F_4TCNQ when heating at elevated temperatures. In stark contrast, the P3MEET:F_4TCNQ blend shows superior thermal stability where the weight loss occurs within the 300−400 °C range.

The lack of weight loss near the sublimation temperature of neutral F_4TCNQ indicates that P3MEET:F_4TCNQ remains in the charged state. Therefore, the charged species (P3MEET positive polarons and F_4TCNQ anions) exhibit higher thermal stability compared to the neutral molecules and thus allows for stable conductivity when heated at elevated temperatures.

Multiple factors likely explain the difference in thermal stability of P3MEET:F_4TCNQ and P3MEEMT:F_4TCNQ pairs. One possible explanation for this behavior is the shift in the ionization energy of P3MEET compared to that of P3MEEMT, which not only facilitates the doping process but in turn hinders dedoping due to the large offset between IE of P3MEET and EA of F_4TCNQ. In other words, the electron-donating ability of the oxygen directly attached to the thiophene ring in P3MEET stabilizes the polaron upon doping, enhancing the stability of the P3MEET:F_4TCNQ system. Alternatively, another possible explanation relates to the side-chain segmental mobility. In our previous publication, using a combination of experimental and simulation results, we showed that the insertion of a methyl spacer in the P3MEEMT side chain resulted in a marked enhancement in side-chain segmental mobility compared to P3MEET.[37] We suspect that the higher side-chain segmental mobility in P3MEEMT not only facilitates diffusion of molecular dopants into the film during doping but also accelerates the dedoping process at elevated temperatures.

One final possible explanation could be the favorable interaction between the P3MEET side chain and F_4TCNQ as suggested by MD simulations below, which will eventually lead to the slower evaporation rate of F_4TCNQ and thus superior thermal stability of the P3MEET:F_4TCNQ system. Using the same MD simulation system demonstrated in Figure 5, we look further into the response of each polymer−dopant to F_4TCNQ loading. Shown in Figure 8 is the energy of interaction, E_{int}, between the polymers and F_4TCNQ, normalized to the amount of F_4TCNQ loaded into the system. As seen in Figure 8, until a critical loading of F_4TCNQ into the system, E_{int} for P3MEET is found to be equal to or lower than E_{int} for P3MEEMT. This indicates that P3MEET more favorably interacts with F_4TCNQ and as such should have a lower chemical potential. We hypothesize this favorable interaction between the dopant and the side chain in P3MEET imparts polymer/dopant miscibility and hence enhances the thermal stability of the P3MEET:F_4TCNQ system.

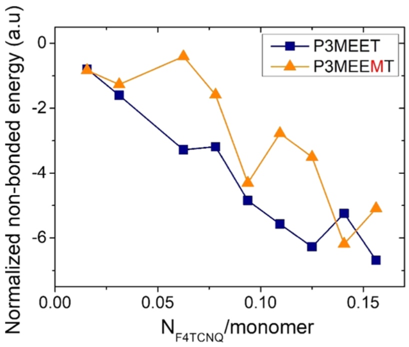

Figure 8. MD simulation results of side-chain/F_4TCNQ nonbond energy E_{int} as a function of F_4TCNQ to monomer ratio.

3. CONCLUSIONS

In conclusion, we investigated the role of polar side-chain chemistry in molecular doping efficiency, conductivity, and thermal stability through two polythiophene derivatives, P3MEET and P3MEEMT, upon doping with the molecular dopants F_1TCNQ, F_2TCNQ, and F_4TCNQ. Both polymers possessed oligoethylene glycol polar side chains with their only difference being a methyl spacer between the oxygen and the thiophene in P3MEEMT. The values of σ are within the same order of magnitude for all three fluorinated dopants for the P3MEET polymer, while σ of P3MEEMT decreases significantly with the decreasing fluorination level of dopants, consistent with the polymer−dopant energy level mismatch as suggested by CV measurements. Despite the similarity in their chemical structures, P3MEET exhibited much higher electronic conductivity upon vapor doping with F_nTCNQ and superior thermal stability compared to that of P3MEEMT. Using a combination of experimental and MD simulation approaches, we showed that the enhanced conductivity in P3MEET compared to P3MEEMT likely originated from better doping efficiency of the dopant in P3MEET and higher degree of conformational order of polymer chains in the amorphous domain. Meaning, efficient doping in P3MEET led to higher carrier concentration and the further stiffening of polymer chains in the amorphous domain provides for a higher charge carrier mobility. Though the doping efficiency differences appear clear, the reason for the variation in enhanced thermal stability in P3MEET:F_nTCNQ could originate from several factors. First, the low IE imparted from the placement of the oxygen atom next to the thiophene core could stabilize the polaron formed upon doping, thus hindering the dedoping process. Second, the low segmental mobility of the side chain in P3MEET might result in the slow diffusion of F_4TCNQ and consequently slower sublimation rate. Finally, the favorable side-chain-dopant interaction could enhance the intermixing between P3MEET:F_nTCNQ pairs and their thermal stability. While additional work is needed to decipher the exact mechanism of enhanced thermal stability in doped P3MEET, our data suggested that in contrast to previous beliefs, the use of a polar side-chain alone is not sufficient to achieve high conductivity and thermal stability in molecularly doped CPs. Future design of side chains for high performing materials should take into consideration factors such as side-chain segmental mobility, side-chain−dopant interaction, and the influence of dopants on the semicrystalline structure of the polymers.

4. EXPERIMENTAL SECTION

4.1. Materials and Sample Preparation. Poly(3-(methoxyethoxyethoxy)thiophene) (P3MEET) and poly(3-(methoxyethoxyethoxymethyl)thiophene) (P3MEEMT) were synthesized by first synthesizing the monomers 2,5-dibromo-3-(methoxyethoxyethoxy)thiophene [3MEET] and 2,5-dibromo-3-(methoxyethoxyethoxymethyl)thiophene [3MEEMT] and then polymerizing using Kumada catalyst transfer polymerization (KCTP). Additional synthetic details are provided in our previous publication[37] and in the Supporting Information.

All substrates used in this study were cleaned by ultrasonication in acetone and 2-propanol for 15 min in each solvent, followed by ozone−plasma treatment for 3 min. Grazing-incidence wide-angle X-ray scattering (GIWAXS) and spectroscopic ellipsometry measurements were performed on films deposited on Si substrates with 1.5 nm of native SiO_2. UV−vis spectroscopy, electron paramagnetic resonance (EPR), and four-point probe conductivity measurements were performed on films deposited on quartz substrates. Electronic conductivity measurements were also performed on films deposited atop custom-fabricated interdigitated gold electrodes (IDEs) on Si substrates possessing 1000 nm of thermally grown SiO_2.

Solutions of P3MEET and P3MEEMT were prepared by dissolving the materials in anhydrous chloroform and anhydrous acetonitrile, respectively, at a concentration of 10 mg/mL and stirring overnight before being filtered through a 0.45 μm filter. The solutions were then spin-casted under an argon atmosphere onto the prepared substrates at 2000 rpm for 2 min. Film thicknesses of all samples in this study were kept at ca. 50 nm, as confirmed by spectroscopic ellipsometry measurements.

4.2. Vapor Doping Procedure for Molecular Dopants. Vapor doping of F_nTCNQ (n = 1, 2, 4) was performed using the previously described procedure.[24] In brief, polymer thin films were vapor-doped with F_nTCNQ in an argon-filled glovebox. Approximately 5 mg of dopant was placed in a glass cylinder (diameter, ~5 cm; height, ~4.5 cm), and then, the glass cylinder was inserted into a preheated stainless steel container for at least 30 min on top of a hotplate. Due to the difference in sublimation temperature of each dopant, the temperature of the hotplate was set to 220, 200, and 180 °C for F_4TCNQ, F_2TCNQ, and F_1TCNQ, respectively. During the vapor doping process, the thin film sample was placed upside down above the glass jar. The sample was kept at a constant temperature of 50 °C during the doping process using a custom-built thermoelectric module.

4.3. Electronic Conductivity Calculation. Electronic conductivity was measured either using the four-point probe method (for conductivity above 10^{-3} S/cm) or IDEs (for conductivity below 10^{-3} S/cm). Four-point probe conductivity gold contacts had a channel length of 0.2 mm and a channel width of 1 mm. Four-point probe conductivity measurements were performed using a custom-designed probe station in an argon glovebox. Voltage and current measurements were performed using a Keithley 2400 source measure unit and a Keithley 6221 precision current source. A constant current was applied to the outer contacts, and the resultant steady-state voltage response was recorded from the inside contacts. The resistance (R; Ω) of the sample was extracted from the slope of the VI sweep using Ohm's law ($V = IR$).

IDE conductivity measurements were performed by applying the DC measurement method to samples fabricated atop IDE devices. The extracted resistance R was then used to calculate the sample conductivity σ according to the following equation

$$\sigma = \frac{1}{R}\frac{d}{l(N-1)h}$$

Here, d = 8 μm is the separation distance between electrode contacts, l = 1000 μm is the electrode length, N = 160 is the number of electrodes, and h is the film thickness.

4.4. Grazing-Incidence Wide-Angle X-ray Scattering (GIWAXS). GIWAXS measurements were performed at beamline 8-ID-E of the Advanced Photon Source, Argonne National Laboratory with 10.86 keV (λ = 0.11416 nm) synchrotron radiation. Samples were enclosed and measured inside a low vacuum chamber (10^{-3} mbar) to minimize concerns about radiation damage as well as to prevent extraneous scattering from ambient air. The measurement time was chosen to be 10 s/frame. For each sample, three data sets were taken from three adjacent spots on the sample and then summed to enhance the signal-to-noise ratio. In our work, the samples were tilted at an angle of incidence of 0.14° with respect to the incoming beam. This angle was chosen to be above the estimated critical angle of the sample (ca. 0.13°) but below the critical angle of the Si substrates (ca. 0.17°). The scattering signal was recorded with a Pilatus 1MF pixel array detector (pixel size = 172 μm) positioned 228 mm from the sample. Each data set was stored as a 981 × 1043 32-bit tiff image with a 20-bit dynamic range. The Pilatus detector has rows of inactive pixels at the border between detector modules. To fill these gaps, after each measurement, the detector was moved to a new vertical direction and the measurement on each spot was repeated; then, the gaps were filled by combining the data from two detector positions. The signals were reshaped and output as intensity maps in q_z vs q_r ($= \sqrt{q_x^2 + q_y^2}$) space. We also performed detector nonuniformity, detection efficiency, the polarization effect, and solid-angle variation for each image. Vertical linecuts were performed as a function of intensity along the q_z direction. All of the GIWAXS data processing and extraction were executed using the GIXSGUI package for MATLAB.[59]

We calculated the side-chain distance, π-stacking distance in P3MEET, and π-stacking in P3MEEMT by analyzing vertical linecuts of GIWAXS patterns but calculated the side-chain distance in P3MEEMT by analyzing horizontal linecuts of GIWAXS patterns. This was due to the more favorable in-plane orientation of the P3MEEMT side chain, which gave rise to a stronger side-chain diffraction signal in horizontal linecuts compared to vertical linecuts. Each linecut was subjected to an empirical baseline subtraction before fitting with a Voigt function to compute the peak position and side-chain or π-stacking distance according to $d = 2\pi/q$.

4.5. UV−Vis−NIR Absorption Spectroscopy. The UV−vis−NIR absorption spectroscopy measurements were performed using a Shimadzu UV-3600 Plus UV−vis−NIR dual-beam spectrophotometer at the Soft Matter Characterization Facility (SMCF) at the University of Chicago.

4.6. Electron Paramagnetic Resonance (EPR) Spectroscopy. Continuous-wave (CW) X-band (9−10 GHz) EPR experiments were carried out with a Bruker ELEXSYS II E500 EPR spectrometer (Bruker Biospin, Rheinstetten, Germany), equipped with a TE_{102} rectangular EPR resonator (Bruker ER 4102ST). Measurements were performed at room temperature (T = 295 K). Thin films on the substrate with dimensions 2 mm × 15 mm^2 were placed in the EPR quartz tubes with 4 mm i.d. For spin quantification, a single crystal of $CuSO_4 \cdot H_2O$ with known spin concentration was used as a reference sample. Spin quantifications were done by comparing double integrals of the experimental and reference EPR signals. For EPR measurement, we estimate a relative error of ca. 20% for each sample due to variations from experimental conditions.

4.7. Raman Spectroscopy. Raman spectroscopy experiments were performed under ambient conditions using a Horiba LabRAM HR Evolution NIR confocal Raman microscope housed in Chicago Materials Research Center. Raman spectra of neat and doped P3MEET and P3MEEMT thin films were collected using a 100× objective at three different excitation wavelengths, 633, 532, and 473 nm. The spatial resolution of each measurement is dependent on the numerical aperture of the microscope objective, the wavelength of the laser used, and the pinhole size of the confocal imaging mode. In our configurations, the spatial resolution of each Raman spectrum is calculated to be less than 1 mm. Laser power and accumulation time were set to 1% and 20 s to minimize local heating and material degradation.

4.8. Thermogravimetric Analysis (TGA). Polymer/dopant blends for TGA analysis were prepared by mixing P3MEET and P3MEEMT solution with F_4TCNQ solution and then the mixed solution was freeze-dried to remove the solvents. P3MEET was dissolved in chloroform, whereas P3MEEMT and F_4TCNQ were dissolved in acetonitrile. TGA measurements were using a discovery thermogravimetric analyzer at the Soft Mater Characterization Facility (SMCF) at the University of Chicago. All TGA samples were measured under a constant flow of N_2 gas and a heating rate of 10 °C/min.

ASSOCIATED CONTENT

Supporting Information

The Supporting Information is available free of charge at https://pubs.acs.org/doi/10.1021/acs.chemmater.0c04153.

Synthesis details of P3MEET and P3MEEMT; CV data of P3MEET, P3MEEMT, F_1TCNQ, F_2TCNQ, and F_4TCNQ; additional GIWAXS data, including raw GIWAXS images of F_4TCNQ-doped samples, pole figure analysis, linecuts of GIWAXS images before and after doping with F_4TCNQ; linecuts of GIWAXS images at different X-ray incidence angles; raw EPR spectra; thermal stability data in ambient air at different temperatures; solution/solid-state absorption spectra of P3MEET and P3MEEMT; and MD simulation details (PDF)

AUTHOR INFORMATION

Corresponding Author

Shrayesh N. Patel − *Pritzker School of Molecular Engineering, University of Chicago, Chicago, Illinois 60637, United States;* orcid.org/0000-0003-3657-827X;
Email: shrayesh@uchicago.edu

Authors

Ban Xuan Dong − *Pritzker School of Molecular Engineering, University of Chicago, Chicago, Illinois 60637, United States;* orcid.org/0000-0002-2873-5207
Christian Nowak − *School of Chemical and Biomolecular Engineering, Cornell University, Ithaca, New York 14953, United States*
Jonathan W. Onorato − *Department of Materials Science and Engineering, University of Washington, Seattle, Washington 98195, United States;* orcid.org/0000-0003-1349-8277
Tengzhou Ma − *Pritzker School of Molecular Engineering, University of Chicago, Chicago, Illinois 60637, United States;* orcid.org/0000-0002-9116-5518
Jens Niklas − *Chemical Sciences and Engineering Division, Argonne National Laboratory, Lemont, Illinois 60439, United States;* orcid.org/0000-0002-6462-2680
Oleg G. Poluektov − *Chemical Sciences and Engineering Division, Argonne National Laboratory, Lemont, Illinois 60439, United States;* orcid.org/0000-0003-3067-9272
Garrett Grocke − *Pritzker School of Molecular Engineering, University of Chicago, Chicago, Illinois 60637, United States;* orcid.org/0000-0001-8661-5038
Mark F. DiTusa − *Pritzker School of Molecular Engineering, University of Chicago, Chicago, Illinois 60637, United States*
Fernando A. Escobedo − *School of Chemical and Biomolecular Engineering, Cornell University, Ithaca, New York 14953, United States;* orcid.org/0000-0002-4722-9836
Christine K. Luscombe − *Department of Materials Science and Engineering, Department of Chemistry, and Molecular Engineering & Sciences Institute, University of Washington, Seattle, Washington 98195, United States;* orcid.org/0000-0001-7456-1343
Paul F. Nealey − *Pritzker School of Molecular Engineering, University of Chicago, Chicago, Illinois 60637, United States;* orcid.org/0000-0003-3889-142X

Complete contact information is available at:
https://pubs.acs.org/10.1021/acs.chemmater.0c04153

Notes

The authors declare no competing financial interest.

ACKNOWLEDGMENTS

This work was supported by NSF DMREF Award number 1922259. This research used resources of the Advanced Photon Source, an Office of Science User Facility operated for the U.S. Department of Energy (DOE) by Argonne National Laboratory under Contract no. DE-AC02-06CH11357. The EPR work was supported by the U.S. Department of Energy (DOE), Office of Basic Energy Sciences, Division of Chemical Sciences, Geosciences, and Biosciences, under Contract no. DE-AC-02-06CH11357. Part of this work was carried out at the Soft Matter Characterization Facility of the University of Chicago. This work made use of the Pritzker Nanofabrication Facility, which receives partial support from the SHyNE Resource, a node of the National Science Foundation's National Nanotechnology Coordinated Infrastructure (NSF ECCS-2025633).

REFERENCES

(1) Borsenberger, P. M.; Weiss, D. S. *Organic Photoreceptors for Xerography*; CRC Press: New York, 1998; pp 1−755.

(2) Geffroy, B.; le Roy, P.; Prat, C. Organic Light-Emitting Diode (OLED) Technology: Materials, Devices and Display Technologies. *Polym. Int.* **2006**, *55*, 572−582.

(3) Müllen, K.; Scherf, U. *Organic Light Emitting Devices: Synthesis, Properties and Applications*; Wiley: New York, 2006; pp 1−410.

(4) Sirringhaus, H. 25th Anniversary Article: Organic Field-Effect Transistors: The Path Beyond Amorphous Silicon. *Adv. Mater.* **2014**, *26*, 1319−1335.

(5) Günes, S.; Neugebauer, H.; Sariciftci, N. S. Conjugated Polymer-Based Organic Solar Cells. *Chem. Rev.* **2007**, *107*, 1324−1338.

(6) Kroon, R.; Lenes, M.; Hummelen, J. C.; Blom, P. W. M.; de Boer, B. Small Bandgap Polymers for Organic Solar Cells (Polymer Material Development in the Last 5 Years). *Polym. Rev.* **2008**, *48*, 531−582.

(7) Loiudice, A.; Rizzo, A.; Biasiucci, M.; Gigli, G. Bulk Heterojunction versus Diffused Bilayer: The Role of Device Geometry in Solution p-Doped Polymer-Based Solar Cells. *J. Phys. Chem. Lett.* **2012**, *3*, 1908−1915.

(8) Zhang, Y.; Zhou, H.; Seifter, J.; Ying, L.; Mikhailovsky, A.; Heeger, A. J.; Bazan, G. C.; Nguyen, T.-Q. Molecular Doping Enhances Photoconductivity in Polymer Bulk Heterojunction Solar Cells. *Adv. Mater.* **2013**, *25*, 7038−7044.

(9) Yan, H.; Manion, J. G.; Yuan, M.; García de Arquer, F. P.; McKeown, G. R.; Beaupré, S.; Leclerc, M.; Sargent, E. H.; Seferos, D. S. Increasing Polymer Solar Cell Fill Factor by Trap-Filling with F4-TCNQ at Parts Per Thousand Concentration. *Adv. Mater.* **2016**, 6491−6496.

(10) Lu, G.; Blakesley, J.; Himmelberger, S.; Pingel, P.; Frisch, J.; Lieberwirth, I.; Salzmann, I.; Oehzelt, M.; Di Pietro, R.; Salleo, A.; et al. Moderate Doping Leads to High Performance of Semiconductor/Insulator Polymer Blend Transistors. *Nat. Commun.* **2013**, *4*, No. 1588.

(11) Lüssem, B.; Keum, C. M.; Kasemann, D.; Naab, B.; Bao, Z.; Leo, K. Doped Organic Transistors. *Chem. Rev.* **2016**, *116*, 13714−13751.

(12) Bubnova, O.; Crispin, X. Towards Polymer-Based Organic Thermoelectric Generators. *Energy Environ. Sci.* **2012**, *5*, 9345−9362.

(13) Russ, B.; Glaudell, A.; Urban, J. J.; Chabinyc, M. L.; Segalman, R. A. Organic Thermoelectric Materials for Energy Harvesting and Temperature Control. *Nat. Rev. Mater.* **2016**, *1*, No. 16050.

(14) Patel, S. N.; Chabinyc, M. L. Anisotropies and the Thermoelectric Properties of Semiconducting Polymers. *J. Appl. Polym. Sci.* **2017**, *134*, No. 44403.

(15) Kang, K.; Watanabe, S.; Broch, K.; Sepe, A.; Brown, A.; Nasrallah, I.; Nikolka, M.; Fei, Z.; Heeney, M.; Matsumoto, D.; et al. 2D Coherent Charge Transport in Highly Ordered Conducting Polymers Doped by Solid State Diffusion. *Nat. Mater.* **2016**, *15*, 896−902.

(16) Jacobs, I. E.; Aasen, E. W.; Oliveira, J. L.; Fonseca, T. N.; et al. Comparison of Solution-Mixed and Sequentially Doping-Induced Aggregation on Film Morphology. *J. Mater. Chem. C* **2016**, *4*, 3454−3466.

(17) Scholes, D. T.; Hawks, S. A.; Yee, P. Y.; Wu, H.; Lindemuth, J. R.; Tolbert, S. H.; Schwartz, B. J. Overcoming Film Quality Issues for Conjugated Polymers Doped with F4TCNQ by Solution Sequential Processing: Hall Effect, Structural, and Optical Measurements. *J. Phys. Chem. Lett.* **2015**, *6*, 4786−4793.

(18) Patel, S. N.; Javier, A. E.; Beers, K. M.; Pople, J. A.; Ho, V.; Segalman, R. A.; Balsara, N. P. Morphology and Thermodynamic Properties of a Copolymer with an Electronically Conducting Block: Poly(3-Ethylhexylthiophene)-Block-Poly(Ethylene Oxide). *Nano Lett.* **2012**, *12*, 4901−4906.

(19) Lim, E.; Peterson, K. A.; Su, G. M.; Chabinyc, M. L. Thermoelectric Properties of Poly(3-Hexylthiophene) (P3HT) Doped with 2,3,5,6-Tetrafluoro-7,7,8,8-Tetracyanoquinodimethane (F4TCNQ) by Vapor-Phase Infiltration. *Chem. Mater.* **2018**, *30*, 998−1010.

(20) Hynynen, J.; Kiefer, D.; Yu, L.; Kroon, R.; Munir, R.; Amassian, A.; Kemerink, M.; Müller, C. Enhanced Electrical Conductivity of Molecularly P-Doped Poly(3-Hexylthiophene) through Understanding the Correlation with Solid-State Order. *Macromolecules* **2017**, *50*, 8140−8148.

(21) Dong, B. X.; Liu, Z.; Misra, M.; Strzalka, J.; Niklas, J.; Poluektov, O.; Escobedo, F. A.; Ober, C. K.; Nealey, P. F.; Patel, S. N. Structure Control of a π-Conjugated Oligothiophene-Based Liquid Crystal for Enhanced Mixed Ion/Electron Transport Characteristics. *ACS Nano* **2019**, *13*, 7665−7675.

(22) Gao, J.; Stein, B. W.; Thomas, A. K.; Garcia, J. A.; Yang, J.; Kirk, M. L.; Grey, J. K. Enhanced Charge Transfer Doping Efficiency in J-Aggregate Poly(3-Hexylthiophene) Nanofibers. *J. Phys. Chem. C* **2015**, *119*, 16396−16402.

(23) Salzmann, I.; Heimel, G.; Oehzelt, M.; Winkler, S.; Koch, N. Molecular Electrical Doping of Organic Semiconductors: Fundamental Mechanisms and Emerging Dopant Design Rules. *Acc. Chem. Res.* **2016**, *49*, 370−378.

(24) Patel, S. N.; Glaudell, A. M.; Peterson, K. A.; Thomas, E. M.; O'Hara, K. A.; Lim, E.; Chabinyc, M. L. Morphology Controls the Thermoelectric Power Factor of a Doped Semiconducting Polymer. *Sci. Adv.* **2017**, *3*, No. e1700434.

(25) Ma, T.; Dong, B. X.; Grocke, G. L.; Strzalka, J.; Patel, S. N. Leveraging Sequential Doping of Semiconducting Polymers to Enable Functionally Graded Materials for Organic Thermoelectrics. *Macromolecules* **2020**, *53*, 2882−2892.

(26) Scholes, D. T.; Yee, P. Y.; Lindemuth, J. R.; Kang, H.; Onorato, J.; Ghosh, R.; Luscombe, C. K.; Spano, F. C.; Tolbert, S. H.; Schwartz, B. J. The Effects of Crystallinity on Charge Transport and the Structure of Sequentially Processed F4TCNQ-Doped Conjugated Polymer Films. *Adv. Funct. Mater.* **2017**, *27*, No. 1702654.

(27) Hamidi-Sakr, A.; Biniek, L.; Bantignies, J. L.; Maurin, D.; Herrmann, L.; Leclerc, N.; Lévêque, P.; Vijayakumar, V.; Zimmermann, N.; Brinkmann, M. A Versatile Method to Fabricate Highly In-Plane Aligned Conducting Polymer Films with Anisotropic Charge Transport and Thermoelectric Properties: The Key Role of Alkyl Side Chain Layers on the Doping Mechanism. *Adv. Funct. Mater.* **2017**, *27*, No. 1700173.

(28) Glaudell, A. M.; Cochran, J. E.; Patel, S. N.; Chabinyc, M. L. Impact of the Doping Method on Conductivity and Thermopower in Semiconducting Polythiophenes. *Adv. Energy Mater.* **2015**, *5*, No. 1401072.

(29) Schlitz, R. A.; Brunetti, F. G.; Glaudell, A. M.; Miller, P. L.; Brady, M. A.; Takacs, C. J.; Hawker, C. J.; Chabinyc, M. L. Solubility-Limited Extrinsic n-Type Doping of a High Electron Mobility Polymer for Thermoelectric Applications. *Adv. Mater.* **2014**, *26*, 2825−2830.

(30) Vijayakumar, V.; Zhong, Y.; Untilova, V.; Bahri, M.; Herrmann, L.; Biniek, L.; Leclerc, N.; Brinkmann, M. Bringing Conducting Polymers to High Order: Toward Conductivities beyond 10 5 S Cm −1 and Thermoelectric Power Factors of 2 MW m −1 K −2. *Adv. Energy Mater.* **2019**, No. 1900266.

(31) Li, J.; Rochester, C. W.; Jacobs, I. E.; Aasen, E. W.; Friedrich, S.; Stroeve, P.; Moulé, A. J. The Effect of Thermal Annealing on Dopant Site Choice in Conjugated Polymers. *Org. Electron.* **2016**, *33*, 23−31.

(32) Li, J.; Rochester, C. W.; Jacobs, I. E.; Friedrich, S.; Stroeve, P.; Riede, M.; Moulé, A. J. Measurement of Small Molecular Dopant F4TCNQ and C60F36 Diffusion in Organic Bilayer Architectures. *ACS Appl. Mater. Interfaces* **2015**, *7*, 28420−28428.

(33) Li, J.; Koshnick, C.; Diallo, S. O.; Ackling, S.; Huang, D. M.; Jacobs, I. E.; Harrelson, T. F.; Hong, K.; Zhang, G.; Beckett, J.; et al. Quantitative Measurements of the Temperature-Dependent Microscopic and Macroscopic Dynamics of a Molecular Dopant in a Conjugated Polymer. *Macromolecules* **2017**, *50*, 5476−5489.

(34) Yamashita, Y.; Tsurumi, J.; Ohno, M.; Fujimoto, R.; Kumagai, S.; Kurosawa, T.; Okamoto, T.; Takeya, J.; Watanabe, S. Efficient Molecular Doping of Polymeric Semiconductors Driven by Anion Exchange. *Nature* **2019**, *572*, 634−638.

(35) Kroon, R.; Kiefer, D.; Stegerer, D.; Yu, L.; Sommer, M.; Müller, C. Polar Side Chains Enhance Processability, Electrical Conductivity, and Thermal Stability of a Molecularly p-Doped Polythiophene. *Adv. Mater.* **2017**, *29*, No. 1700930.

(36) Kiefer, D.; Kroon, R.; Hofmann, A. I.; Sun, H.; Liu, X.; Giovannitti, A.; Stegerer, D.; Cano, A.; Hynynen, J.; Yu, L.; et al. Double Doping of Conjugated Polymers with Monomer Molecular Dopants. *Nat. Mater.* **2019**, *18*, 149−155.

(37) Dong, B. X.; Nowak, C.; Onorato, J. W.; Strzalka, J.; Escobedo, F. A.; Luscombe, C. K.; Nealey, P. F.; Patel, S. N. Influence of Side-Chain Chemistry on Structure and Ionic Conduction Characteristics of Polythiophene Derivatives: A Computational and Experimental Study. *Chem. Mater.* **2019**, *31*, 1418−1429.

(38) Nielsen, C. B.; Giovannitti, A.; Sbircea, D. T.; Bandiello, E.; Niazi, M. R.; Hanifi, D. A.; Sessolo, M.; Amassian, A.; Malliaras, G. G.; Rivnay, J.; et al. Molecular Design of Semiconducting Polymers for High-Performance Organic Electrochemical Transistors. *J. Am. Chem. Soc.* **2016**, *138*, 10252−10259.

(39) Hu, P.; Du, K.; Wei, F.; Jiang, H.; Kloc, C. Crystal Growth, HOMO-LUMO Engineering, and Charge Transfer Degree in Perylene-FxTCNQ (x = 1, 2, 4) Organic Charge Transfer Binary Compounds. *Cryst. Growth Des.* **2016**, *16*, 3019−3027.

(40) Li, J.; Duchemin, I.; Roscioni, O. M.; Friederich, P.; Anderson, M.; Da Como, E.; Kociok-Köhn, G.; Wenzel, W.; Zannoni, C.; Beljonne, D.; et al. Host Dependence of the Electron Affinity of Molecular Dopants. *Mater. Horiz.* **2019**, *6*, 107−114.

(41) Méndez, H.; Heimel, G.; Winkler, S.; Frisch, J.; Opitz, A.; Sauer, K.; Wegner, B.; Oehzelt, M.; Röthel, C.; Duhm, S.; et al. Charge-Transfer Crystallites as Molecular Electrical Dopants. *Nat. Commun.* **2015**, *6*, No. 8560.

(42) Wang, C.; Duong, D. T.; Vandewal, K.; Rivnay, J.; Salleo, A. Optical Measurement of Doping Efficiency in Poly(3-Hexylthiophene) Solutions and Thin Films. *Phys. Rev. B: Condens. Matter Mater. Phys.* **2015**, *91*, No. 085205.

(43) Jacobs, I. E.; Aasen, E. W.; Oliveira, J. L.; Fonseca, T. N.; Roehling, J. D.; Li, J.; Zhang, G.; Augustine, M. P.; Mascal, M.; Moulé, A. J. Comparison of Solution-Mixed and Sequentially Processed P3HT:F4TCNQ FFlms: Effect of Doping-Induced Aggregation on Film Morphology. *J. Mater. Chem. C* **2016**, *4*, 3454−3466.

(44) Coehoorn, R.; Pasveer, W.; Bobbert, P.; Michels, M. Charge-Carrier Concentration Dependence of the Hopping Mobility in Organic Materials with Gaussian Disorder. *Phys. Rev. B* **2005**, *72*, No. 155206.

(45) Li, A.; Dong, B. X.; Green, P. Influence of Morphological Disorder on In- and Out-of-Plane Charge Transport in Conjugated Polymer Films. *MRS Commun.* **2015**, *5*, 593−598.

(46) Dong, B. X.; Li, A.; Strzalka, J.; Stein, G. E.; Green, P. F. Molecular Organization in MAPLE-Deposited Conjugated Polymer Thin Films and the Implications for Carrier Transport Characteristics. *J. Polym. Sci., Part B: Polym. Phys.* **2017**, *55*, 39−48.

(47) Hammond, M. R.; Kline, R. J.; Herzing, A. A.; Richter, L. J.; Germack, D. S.; Ro, H.-W.; Soles, C. L.; Fischer, D. A.; Xu, T.; Yu, L.;

et al. Molecular Order in High-Efficiency Polymer/Fullerene Bulk Heterojunction Solar Cells. *ACS Nano* **2011**, *5*, 8248−8257.

(48) Thomas, E. M.; Brady, M. A.; Nakayama, H.; Popere, B. C.; Segalman, R. A.; Chabinyc, M. L. X-Ray Scattering Reveals Ion-Induced Microstructural Changes During Electrochemical Gating of Poly(3-Hexylthiophene). *Adv. Funct. Mater.* **2018**, No. 1803687.

(49) Thelen, J. L.; Wu, S. L.; Javier, A. E.; Srinivasan, V.; Balsara, N. P.; Patel, S. N. Relationship between Mobility and Lattice Strain in Electrochemically Doped Poly(3-Hexylthiophene). *ACS Macro Lett.* **2015**, *4*, 1386−1391.

(50) Guardado, J. O.; Salleo, A. Structural Effects of Gating Poly(3-Hexylthiophene) through an Ionic Liquid. *Adv. Funct. Mater.* **2017**, *27*, No. 1701791.

(51) Jacobs, I. E.; Cendra, C.; Harrelson, T. F.; Bedolla Valdez, Z. I.; Faller, R.; Salleo, A.; Moulé, A. J. Polymorphism Controls the Degree of Charge Transfer in a Molecularly Doped Semiconducting Polymer. *Mater. Horiz.* **2018**, *5*, 655−660.

(52) Müller, L.; Nanova, D.; Glaser, T.; Beck, S.; Pucci, A.; Kast, A. K.; Schröder, R. R.; Mankel, E.; Pingel, P.; Neher, D.; et al. Charge-Transfer-Solvent Interaction Predefines Doping Efficiency in p-Doped P3HT Films. *Chem. Mater.* **2016**, *28*, 4432−4439.

(53) Liu, W.; Müller, L.; Ma, S.; Barlow, S.; Marder, S. R.; Kowalsky, W.; Köhn, A.; Lovrincic, R. The Origin of the π-π Spacing Change upon Doping of Semiconducting Polymers. *J. Phys. Chem. C* **2018**, 27983.

(54) Schmode, P.; Savva, A.; Kahl, R.; Ohayon, D.; Meichsner, F.; Dolynchuk, O.; Thurn-Albrecht, T.; Inal, S.; Thelakkat, M. The Key Role of Side Chain Linkage in Structure Formation and Mixed Conduction of Ethylene Glycol Substituted Polythiophenes. *ACS Appl. Mater. Interfaces* **2020**, *12*, 13029−13039.

(55) Chew, A. R.; Ghosh, R.; Shang, Z.; Spano, F. C.; Salleo, A. Sequential Doping Reveals the Importance of Amorphous Chain Rigidity in Charge Transport of Semi-Crystalline Polymers. *J. Phys. Chem. Lett.* **2017**, *8*, 4974−4980.

(56) Tsoi, W. C.; James, D. T.; Kim, J. S.; Nicholson, P. G.; Murphy, C. E.; Bradley, D. D. C.; Nelson, J.; Kim, J. S. The Nature of In-Plane Skeleton Raman Modes of P3HT and Their Correlation to the Degree of Molecular Order in P3HT:PCBM Blend Thin Films. *J. Am. Chem. Soc.* **2011**, *133*, 9834−9843.

(57) Lim, E.; Glaudell, A. M.; Miller, R.; Chabinyc, M. L. The Role of Ordering on the Thermoelectric Properties of Blends of Regioregular and Regiorandom Poly(3-Hexylthiophene). *Adv. Electron. Mater.* **2019**, No. 1800915.

(58) Finn, P.; Jacobs, I. E.; Armitage, J.; Wu, R.; Paulsen, B.; Freeley, M.; Palma, M.; Rivnay, J.; Sirringhaus, H.; Nielsen, C. Effect of Polar Side Chains on Neutral and P-Doped Polythiophene. *J. Mater. Chem. C* **2020**, 16216.

(59) Jiang, Z. GIXSGUI: A MATLAB Toolbox for Grazing-Incidence X-Ray Scattering Data Visualization and Reduction, and Indexing of Buried Three-Dimensional Periodic Nanostructured Films. *J. Appl. Crystallogr.* **2015**, *48*, 917−926.